Rock and Soil Mechanics 2026 47(3): 912−928 ISSN 1000−7598
https: //doi.org/10.26599/RSM.2025.94300237 journal homepage: rocksoilmech.whrsm.ac.cn

# Shear behavior of red beds grout-rock interfaces: Effect of grout and rock properties

SHU Xiao-yun[1, 2], TIAN Hong-ming[1, 2], ZHU Zhen-de[1], XU Jian-shu[3], QIU Xin[2], WANG Qing-yong[3], XU Zhi-chao[1], LI Yun-fa[2]

1. College of Civil and Transportation Engineering, Hohai University, Nanjing, Jiangsu 210024, China;

2. State Key Laboratory of Geomechanics and Geotechnical Engineering, Institute of Rock and Soil Mechanics, Chinese Academy of Sciences, Wuhan, Hubei 430071, China

3. Xinjiang Shuifa Construction Group Co., Lid., Urumqi, Xinjiang 830099, China

**Abstract:** Soft rock tunnels in red beds frequently encounter anchor failure issues. Improving the mechanical properties of the red-bed soft rock-grout interface is highly significant for ensuring the stability of anchor support. This study employs laboratory direct shear tests in combination with digital image correlation (DIC) technology to investigate the mechanical properties (peak shear strength $\tau_p$, residual shear strength $\tau_r$, and shear stiffness $k_s$) of the grout-rock interface (GRI) among three typical soft rocks from red beds (red sandstone, mudstone, and grey sandstone) and two grout materials (ordinary Portland cement (OPC) and early high-strength cement (EHC)) under varying curing periods (6 h, 1 d, 2 d, and 7 d). The shear behavior and DIC-based failure mode are analyzed for red beds GRIs. The following key findings were observed: (1) As normal stress increases, both the shear strength ($\tau_p$) and shear stiffness ($k_s$) of the GRI also increase, following the trend: red sandstone > mudstone > grey sandstone. The cohesion values of the red sandstone, mudstone, and green sandstone with the EHC grout-rock interface at 2 days are 2.4, 0.9, and 1.2 MPa, respectively. The corresponding internal friction angles are 57.6°, 38.0°, and 27.0°, respectively. (2) With an increase in curing age, both $\tau_p$ and $k_s$ at the GRI increase non-linearly. EHC exhibited superior bonding performance compared to OPC, with $\tau_p$ reaching 7.9 MPa at 6 h and 90% of the 7-day $\tau_p$ being achieved at 2 d in red sandstone conditions. (3) The OPC-bonded specimens primarily exhibit grout failure near the GRI, whereas the EHC-bonded specimens show rock failure in red sandstone and mudstone conditions, and adhesive failure at the interface in grey sandstone. (4) An empirical model for the shear strength of the GRI in red bed soft rocks is proposed and validated, providing a framework for the rapid and reliable evaluation of anchorage strength in red bed soft rock tunnels.

**Keywords:** red-bed soft rocks; grout-rock interface; shear behavior; curing time; DIC

## 1 Introduction

The red beds are widely distributed around the world, and their rock composition mainly consists of sandstone and conglomerate, with intercalations of siltstone, shale, mudstone, limestone, gypsum, and rock salt. Tunnels excavated in red beds often encounter the hazard of large deformation in soft rocks[1], which poses a significant challenge to the anchorage and support of the tunnel. Chen et al.[2−3] revealed the influence mechanism of the failure of tunnel support structures under weak stratum conditions through random large-deformation simulations and physical model tests, providing an important reference for the failure analysis of anchorage systems in red bed formations. In red bed soft rock tunnel projects, the insufficient bonding strength of the grout-rock interface (GRI) is an important reason for anchorage failure; improving the bonding performance of the GRI is of great significance for ensuring the anchorage and support effect of red bed soft rock tunnels. Studies have shown that the bonding performance of the GRI is closely related to both rock and grout properties; therefore, numerous studies have been carried out by researchers.

The impact of rock properties on the bonding performance of the GRI is primarily reflected in factors such as rock surface roughness, strength, mineral composition, and porosity. Generally, the higher the rock strength, the better the bonding effect of the GRI, such as with schist and granite[4−5], sandstone and shale[6], etc. However, some scholars have reached opposite conclusions. Xu et al.[7] conducted shear experiments with granite, sandstone, limestone, and cement slurry, revealing that a higher rock strength leads to a smaller interface bonding strength. It is evident that the influence of rock properties on the

Received: 29 April 2025 Accepted: 12 September 2025
This work was supported by the Major Project of National Natural Science Foundation of China (42293355), the National Natural Science Foundation of China (U2340229, 42207199), the National Key R&D Program of China (2024YFF0508203), the Key Projects of the Natural Science Foundation of Hubei Province (Qing A) (2025AFA103), the Natural Science Foundation of Xizang Autonomous Region (XZ202401ZR0083) and Zhejiang Provincial Natural Science Foundation of China (ZCLMS25D0201).
First author: SHU Xiao-yun, male, born in 1997, PhD candidate, focusing on anchorage support and yieldable support for large deformation of soft rocks. E-mail: shuxiaoyun211@163.com
Corresponding author: TIAN Hong-ming, male, born in 1985, PhD, Professor, research interests: large squeezing deformation of soft rocks and long-term anchorage support for tunnels. E-mail: hmtian@whrsm.ac.cn

shear strength of the GRI is highly complex. Therefore, evaluating the interface shear strength based solely on rock strength may not be sufficiently accurate. In fact, the bonding process between cement grout and rock mainly involves chemical reactions and cation exchange[8]. The grout can penetrate into the surrounding rock to form a "root pile" effect[9], and it can also effectively interlock and bond with the uneven surface of the surrounding rock[10], providing anchorage force. Therefore, the shear strength of the GRI is not only influenced by rock strength, but is also closely related to the degree of bonding between the grout and the rock.

In addition to surface topography, mineralogical composition significantly influences interfacial bonding. Rocks with higher hydrophilicity and roughness tend to demonstrate greater interface shear strength, with a synergistic effect observed between these two factors[11]. Compared to the dense limestone, porous sandstone allows more grout to penetrate into the rock, resulting in stronger interfacial bonding[12]. Numerous shear experiments[13−14] have demonstrated that the interface shear strength is closely related to the compressive strength ratio of the materials on both sides, the shear strength of the softer side materials, the roughness of the interface, and normal stress. The interface shear strength typically falls between the shear strength of the rock and grout. It can be seen that rock properties significantly affect the shear behavior of the GRI. However, there is still little research on the GRI of red bed soft rocks, and the bonding mechanism between red bed soft rocks and different grouts remains unclear.

The impact of grout properties on the bonding performance of the GRI is mainly reflected in grout strength[15−17], curing age[18], cement particle size[19], fluidity[20], and other factors. Cement-based materials are extensively used for grouting in red beds tunnels, including early high-strength cement (EHC) and ordinary Portland cement (OPC). In this case, the interfacial transition zone (ITZ) between the grout and the rock plays a critical role in determining the shear strength of the GRI. Many microscopic experiments have demonstrated that ITZ is a continuous film of $Ca(OH)_2$ overlain by a parallel array of rod-shaped C-S-H gel particles projecting normal to the interface. Immediately after fresh cement paste is placed in contact with the substrate, the thin lower part of the duplex film consisting of $Ca(OH)_2$ is deposited. Presumably, this is in response to supersaturation of the paste fluid concerning $Ca(OH)_2$ at this stage. Subsequently, the C-S-H gel layer of the duplex film begins to form[21]. In the ITZ, the porosity of the grouted layer is higher, and its mechanical properties are poor, making it a weak zone where GRI damage occurs[22]. Therefore, improving the bonding performance of the GRI mainly includes two approaches: increasing grout strength and improving the mechanical properties in the ITZ.

The grout material exhibits a significant impact on the shear behavior of GRI. A large number of tunnel engineering practices have demonstrated[23] that the OPC grout commonly used in field applications exhibits slow strength development, which often fails to meet the timely anchorage and support requirements in soft rock tunneling. Therefore, engineers have begun to study EHC materials[15−17]. For example, adding 2.0% KBr, 3.0% $Ca(HCOO)_2$[24], propylene-ethylene emulsions[25], and high volumes of fly ash[26] to the cement can effectively improve the early compressive and tensile strength of the grout, thereby enhancing the bonding strength of the GRI. However, shear experiments have shown[27] that the improvement of grout strength has a minimal effect on the improvement of interface bonding properties, and the interface shear strength is mainly influenced by the micro-mechanical properties in the ITZ. Adding fine particle materials to the grout can effectively fill the pores in the ITZ, thereby improving the shear performance of the interface. For example, reducing cement particle size and adding nano-silica can improve the mechanical properties of the ITZ and increase the interface shear strength[6, 19]. The addition of polypropylene fibers[27−28] or sodium sulfate[29] to the cement can improve the density of the ITZ, forming a more efficient fine aggregate-fiber interlocking, and thus enhance the bonding strength of the GRI.

The shear performance of GRI is also influenced by the curing age of cement. As the curing age increases, the amount of hydration products in the grout rises, and the pore structure of the hardened grout becomes progressively denser over time[30−32]. Based on shear tests of the rock-CPB interface, Zhang et al.[33] observed that both adhesion and friction angle increase with extended curing time, while the proportion of macropores and secondary pores in CPB decreases. Ding et al.[34] reported that increasing the curing age enhances the shear strength and stiffness of OPC bonding specimens, and the fractal dimension can be utilized as an indicator for evaluating the shear behavior of GRI. Except for OPC, some time-dependent bonding behavior of EHC has been studied as well. Xue et al.[35] investigated the bonding property of magnesium phosphate fast hardening cement. The results showed that the shear performance increased rapidly before 7 d but slowed significantly after 7 d. Liao et al.[36] proposed a high flowability and stability cement, and found that the electrical resistivity of the hardened grout increased with the curing time and eventually stabilized. With the development of materials science, the performance of grouting materials has been significantly improved. However, their application in red bed soft rock tunnels remains limited, and the bonding performance of GRI under different grout types and curing ages in such geological conditions is still not well understood.

In summary, scholars have conducted valuable research

on the shear mechanical properties of GRIs, but the shear mechanical characteristics of the GRI in red bed soft rocks under different grout types and curing ages remain insufficiently understood. Therefore, this paper selects three typical red bed soft rocks (mudstone, grey sandstone, and red sandstone) and compares the shear mechanical characteristics of the GRI under different curing ages (6 h, 1 d, 2 d, 7 d) and grout types (OPC and EHC) through indoor direct shear tests. Combined with a digital image correlation (DIC) algorithm, the GRI failure characteristics of red bed soft rocks under different conditions are analyzed, and a shear strength prediction model for the GRI is proposed, laying the foundation for the reasonable assessment of anchorage and support effects in red bed soft rock tunnels.

## 2 Materials and experiments

### 2.1 Materials

2.1.1 Property of grout

The EHC formulated in this article primarily consists of ferroaluminate cement (FAC), with appropriate amounts of OPC, dihydrate gypsum, limestone powder, and additives. the mix ratios of the base materials are presented in Table 1. FAC is characterized by a fast setting and hardening speed, while OPC has the property of strength steadily increasing with curing time. The combination of the two ensures the stability of both timely and long-term support for the anchor bolts. Furthermore, OPC not only provides an alkaline environment but also generates hydration products through its reaction with FAC. These products can mutually enhance their hydration processes, thereby accelerating the setting and hardening of the cement. Incorporating an appropriate amount of hard gypsum can prevent the rapid setting of OPC and promote the formation of high-sulfur calcium sulfoaluminate, thus reducing the setting time of FAC. Additionally, adding a certain proportion of limestone can prevent the reduction of flexural strength in cement, promote the hydration heat of FAC, and facilitate the stable formation of calcium carbonate-aluminate compounds in combination with monosulfate calcium aluminate. This synergistic effect further enhances the overall strength and expansion properties of the cement.

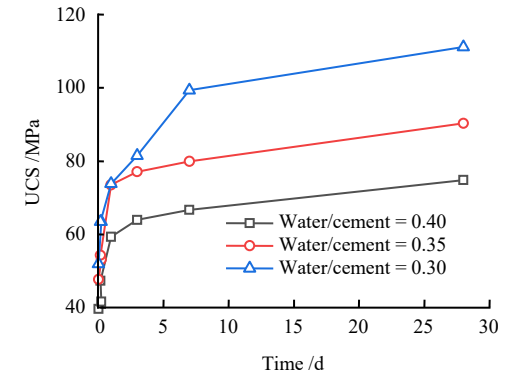
**Table 1 Proportion of basic materials of early high-strength cement**

| Materials | Content /% | Materials | Content /% |
|---|---|---|---|
| FAC | 80 | Dihydrate gypsum | 8 |
| OPC | 7 | Limestone flour | 5 |

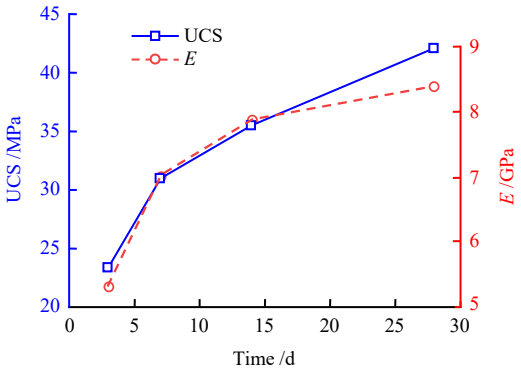
To further promote the setting and hardening of the cement, appropriate amounts of Sika 530p, lithium carbonate, and boric acid were also incorporated. Sika 530p, a polycarboxylate-based superplasticizer, was introduced to improve particle dispersion and reduce water demand while maintaining workability. Lithium carbonate served as a potent accelerator by promoting rapid hydration of $C_3S$ phases through increased hydroxide ion concentration in the pore solution. Boric acid was employed as a setting regulator to prevent flash setting induced by lithium carbonate, as it forms a protective borate layer that moderates the initial hydration rate. This synergistic formulation enabled controlled rapid setting while maintaining sufficient working time and facilitating early strength development. The specific proportions of these additives are shown in Table 2.

**Table 2 Proportion of early high-strength cement admixtures**

| Materials | Content /% | Materials | Content /% |
|---|---|---|---|
| Sika 530p | 0.20 | Defoamer | 0.02 |
| Boric acid | 0.30 | Cellulose | 0.02 |
| Lithium carbonate | 0.01 | | |




(a) EHC




(b) OPC

**Fig. 1 Mechanical properties of EHC and OPC under different curing ages**

The indoor tests show that the prepared EHC has an initial setting time of approximately 20 to 30 minutes, an expansion rate of about $3\times10^{-4}$, and a compressive strength exceeding 30 MPa after 1 hour. After 1 day, the uniaxial compressive strength (UCS) exceeds 60 MPa, as shown in Fig. 1(a). For grout materials used in prestressed anchors, the UCS at 3 days of age should reach 15–20 MPa[37]. The prepared EHC meets the strength requirements for

the design of anchor bolts. The strength of the EHC shows a significant increase in the early stages, with rapid growth observed within the first few days. However, after 3 days, the rate of UCS decreases significantly. The detailed properties of this EHC can be referenced in the previous studies[15−17]. The strength variation trend of the cement with different water-to-cement ratios generally remains consistent. In the experiment, the water-to-cement ratio for the EHC was set at 0.35. To compare the effect of slurry properties, OPC with the same water-to-cement ratio was used. The UCS and elastic modulus of OPC vary with age, as shown in Fig. 1(b).

2.1.2 Property of rock

The study selected three common types of red bed soft rocks as research subjects: mudstone, grey sandstone, and red sandstone. These materials are typically used in geotechnical research due to their distinct characteristics and importance in engineering applications (Table 3). The selected red-bed soft rocks were sourced from the water diversion tunnel of a water diversion project in Xinjiang, China. Their physical and mechanical properties are as follows:

**Table 3 Mineral composition of the testing rocks**

| Rocks | Quartz /% | Feldspar /% | Plagioclase /% | Calcite /% | Dolomite /% | Sum of minor minerals /% |
|---|---|---|---|---|---|---|
| Mudstone | 21.4 | 0.5 | 10.9 | 11.4 | 1.5 | 52.5 |
| Red sandstone | 74.4 | 11.9 | 1.3 | 1.4 | 0.7 | 10.3 |
| Grey sandstone | 77.7 | 10.4 | 0.98 | 1.4 | 0.6 | 8.9 |

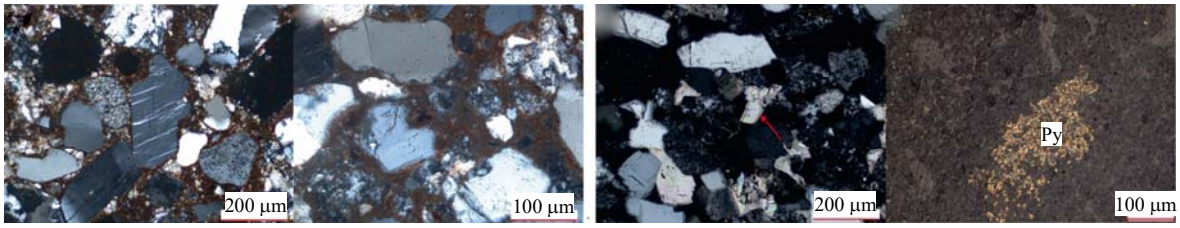
As shown in Fig. 2(a), the mudstone is brownish-red in color, with a clayey cementation, and locally contains small amounts of calcareous nodules. The mudstone has a montmorillonite content exceeding 16.15%, with a softening coefficient of 0.35. The average UCS in its natural state is 2.77 MPa. After soaking in water for 1.5 hours, the UCS decreases to 0.25 MPa. The elastic modulus is 0.6 GPa, and the Poisson's ratio is 0.37. These characteristics classify it as an extremely soft rock. (JRC) of the mudstone is approximately between 0 and 3.



(a) Mudstone (b) Red sandstone (c) Grey sandstone

**Fig. 2 Specimen of rocks**

As shown in Fig. 2(b), the red sandstone has an average longitudinal wave velocity of approximately 2.9 km/s, a porosity ranging from 8% to 15%, and a saturation water absorption rate of 2.96%. The average density of the dry sample is 2.40 g/cm³, the cohesion is 6.2 MPa, the internal friction angle is 29.2°, and the elastic modulus is 14.2 GPa. The average density of the saturated sample is 2.47 g/cm³, the cohesion is 6.02 MPa, the internal friction angle is 24.2°, and the elastic modulus is 10.29 GPa, classifying it as soft rock. The roughness coefficient is approximately 3 to 5. In red sandstone, the interstitial material is mainly a dark brownish-red or brownish-red matrix filled around or between mineral particles (Fig. 3(a) and Fig. 3(b))[39].




(a) Red sandstone, ×500 (b) Red sandstone, ×1 000 (c) Grey sandstone, ×500 (d) Grey sandstone, ×1 000

**Fig. 3 Typical micrographs of grey and red sandstones (Jiang et al., 2024)**

As shown in Fig. 2(c), the grey sandstone is light gray, with local inclusions of quartz gravel, with a particle size of 0.5−2 mm and a porosity of 5−8%. Using the average dry bulk density of 2.42 g/cm³, the initial water content was estimated to be approximately 0.78%[40]. The content of montmorillonite in the grey sandstone is

less than 10%, the average compressive strength under saturation is 8.2 MPa, the elastic modulus is 71 GPa, and the Poisson's ratio is 0.2, classifying it as soft rock. The roughness coefficient is approximately between 0 and 3. In grey sandstone, mineral particles are predominantly filled with dark matrix (Fig. 3(c)), and iron primarily exists in the form of pyrite (Fig. 3(d)), resulting in a lack of deep brownish-red or reddish-brown minerals in the matrix[38].

## 2.2 Experimental programs

### 2.2.1 Specimen preparation

(1) Rock preparation: The mudstone, grey sandstone, and red sandstone samples collected from the field are cut into rectangular blocks with dimensions of 100 mm× 100 mm×50 mm. Subsequently, the surfaces of the samples are polished to ensure that perpendicularity and parallelism deviations remain within 0.02 mm. All specimens are subjected to rigorous quality assessment via ultrasonic wave velocity measurements. Specimens exhibiting significant variations in wave velocity are removed to ensure specimen consistency and reliability. The surrounding rock is placed at the bottom of a 100 mm×100 mm× 100 mm mold, as shown in Fig. 4(a). Finally, grease was applied along the mold joints to prevent grout leakage during the pouring process.

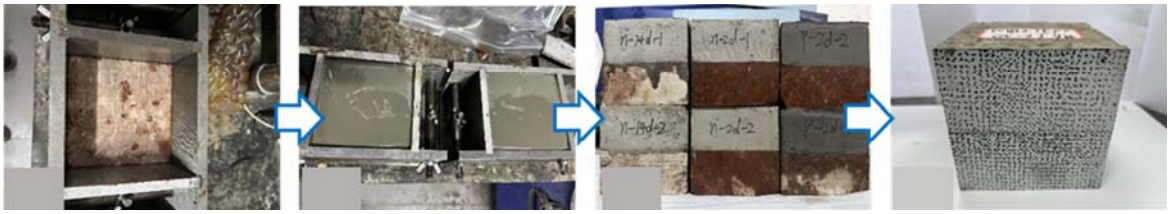
(2) Sample preparation: According to the material proportions shown in Table 1 and Table 2, the required materials were weighed according to the predetermined mass and mixed by an NJ-160A cement slurry mixer. Sample preparation was conducted in accordance with the *Cement Mortar Strength Testing Method* (ISO Method) (GB/T 17671—2020). Initially, the materials are mixed slowly for 90 seconds, followed by a 30-second pause. Subsequently, they are mixed rapidly for 60 seconds. Thereafter, the cement slurry is poured into the designated mold and bonded with the surrounding rock, as illustrated in Fig. 4(b). After pouring, the sample is placed in a standard curing chamber to prevent moisture loss.

(3) Sample curing: After curing for 24 hours in a standard curing box, the mold is removed. Then, the sample is placed in a standard curing room (temperature 20 ± 2 ºC) until different ages, as shown in Fig. 4(c).

(4) Spot pattern creation: Matte spray paint was applied at an obliquely upward angle, approximately 30 cm away from the sample. This allows the spots to fall freely onto the surface of the tested sample, as shown in Fig. 4(d). After the spot pattern creation is completed, the VIC-Snap image acquisition software is used to assess the quality of the speckle pattern. This software allows for precise evaluation of the speckle quality, ensuring that the pattern is suitable for the intended testing or measurement purposes.

The experimental design is shown in Table 4. #1 and #2 respectively conduct shear tests on the bond samples between EHC and OPC with red sandstone at 6 hours, 1 day, 2 days, and 7 days. The normal stress applied to the samples is 4 MPa. The primary focus of the analysis is on how the grout properties affect the GRI shear behavior. #3, #4, and #5 respectively conduct shear tests on the bond samples between red sandstone, mudstone, and grey sandstone with EHC at 2 days. The normal stress applied to the samples is 1, 2, 3, and 4 MPa. The primary focus of the analysis is on how the rock properties affect the GRI shear behavior.

In this study, three specimens were prepared for each experimental group (#1 to #5) to minimize experimental random errors. To ensure data reliability, a systematic approach was employed for outlier identification. Specimens exhibiting a coefficient of variation (COV) exceeding 15% within any test group were considered outliers and excluded from further analysis. The remaining specimens were subsequently re-evaluated, and if at least two consistent results (COV≤15%) were obtained, they were used for subsequent analysis. This quality control procedure ensured the statistical validity of the experimental results while accounting for inherent material heterogeneity.



(a) Mold preparation (b) Cement pouring (c) Specimen curing (d) Speckle fabrication

**Fig. 4 Preparation of grout-rock composite specimens**

**Table 4 Design of shear test scheme**

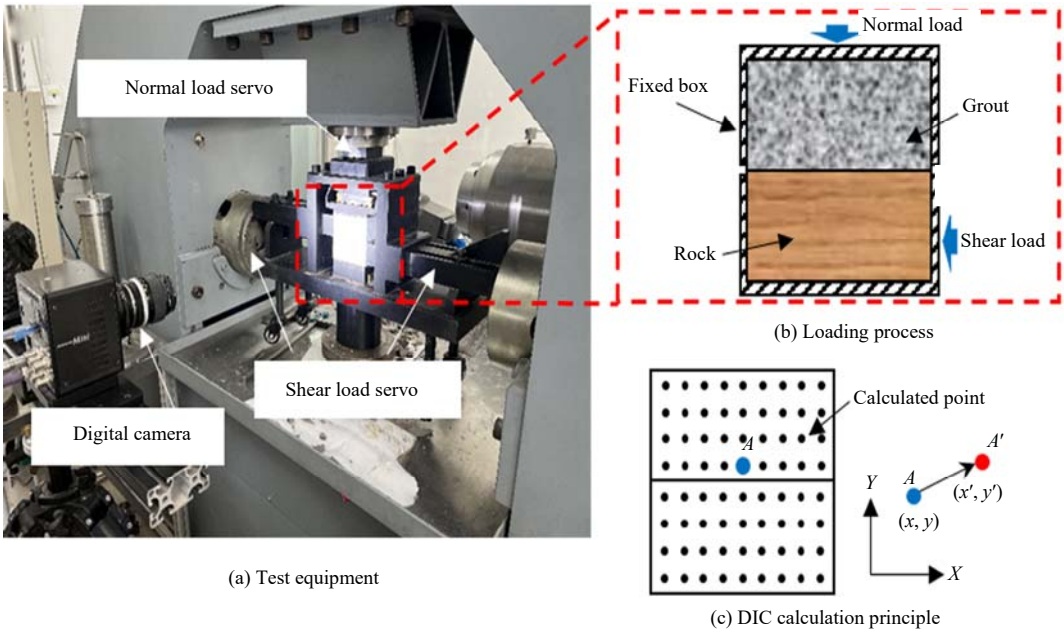
| Class | Grout | Rocks | Curing time | Normal stress /MPa |
|---|---|---|---|---|
| #1 | OPC | Red sandstone | 6 h, 1 d, 2 d, 7 d | 4 |
| #2 | EHC | Red sandstone | 6 h, 1 d, 2 d, 7 d | 4 |
| #3 | EHC | Red sandstone | 2 d | 1, 2, 3, 4 |
| #4 | EHC | Mudstone | 2 d | 1, 2, 3, 4 |
| #5 | EHC | Grey sandstone | 2 d | 1, 2, 3, 4 |

### 2.2.2 Testing Procedure

This study adopted the rock joint surface stress-seepage coupled shear rheological testing system developed by the Institute of Rock and Soil Mechanics, Chinese Academy of Sciences, Wuhan, to perform direct shear tests, as shown in Fig. 5. This apparatus is specifically designed to study the coupled effects of stress and seepage on rock joint surfaces during shear testing, providing more accurate

and comprehensive data on the shear behavior and characteristics of the materials being tested. The instrument has a maximum normal load of 1 000 kN and a maximum shear displacement of 20 mm. It is capable of applying two types of loading conditions: constant normal stress and constant normal displacement. These loading conditions allow for a more controlled and accurate simulation of different in-situ stress and displacement environments, ensuring that the tests can replicate various real-world conditions for rock joints under shear stress. The experimental process is as follows: (1) Pre-loading: Apply normal stress at a rate of 50 kN/min until it reaches 2 kN, then apply shear stress at the same loading rate of 50 kN/min until it reached 2 kN, ensuring the sample makes complete contact with the loading surface. (2) Normal loading: Apply normal stress at a rate of 50 kN/min until it reaches the designed value (1, 2, 3, 4 MPa), and maintain the normal stress constant. (3) Shear loading: Maintain the normal stress constant, apply shear loading to the sample at a rate of 1 mm/min until the shear displacement reaches 10 mm, at which point the test is terminated. The shear load, shear displacement, and normal displacement were monitored throughout the shear process.

In this study, the DIC algorithm is selected for digital




(a) Test equipment

(b) Loading process

(c) DIC calculation principle

**Fig. 5 Schematic of the test process**

photogrammetry analysis. The schematic of the fundamental steps involved in the DIC algorithm is shown in Fig. 5(c). Before the experiment begins, the observation surface of the sample needs to be marked with speckles, as shown in Fig. 4(d). During the experiment, a high-speed camera is used to capture the shear loading process of the sample in real-time. The obtained digital images are then imported into the DIC software for analysis. During the DIC calculation, the software will identify and mark the calculation points on the observed surface. It tracks and calculates the difference between the coordinates of each point after deformation ($x'$, $y'$) and the coordinates before deformation ($x$, $y$). This process allows for the determination of the displacement and strain field variations across the entire observed surface over time. The software employed for DIC analysis in this study is an open-source MATLAB program named Ncoor v1.2 with a measurement accuracy of approximately 0.01 pixels. To minimize image processing errors, a mirrorless interchangeable lens camera, the Canon 90D, equipped with the Canon EF-S 18–135 mm f/3.5–5.6 IS USM lens, was positioned 100 cm from the specimen. The deformation images of the cement-rock composites were collected with a frame rate of 50 and a resolution of 3 840 × 2 160 pixels.

## 3 Results

The shear stress-displacement curves of GRI at different red beds rock conditions exhibit similarities and can generally be divided into three stages, as shown in Fig. 6:

Elastic Deformation Stage (I): During this stage, the shear stress of the sample increases linearly with the shear displacement. The slope of the curve represents the shear stiffness $k_s$, which indicates the sample's resistance to shear deformation. The shear stiffness $k_s$ can be defined as:

$$k_s = \frac{\Delta\tau}{\Delta\delta} \tag{1}$$

where $\Delta\tau$ and $\Delta\delta$ are the increments of shear stress and shear displacement in the elastic deformation stage.

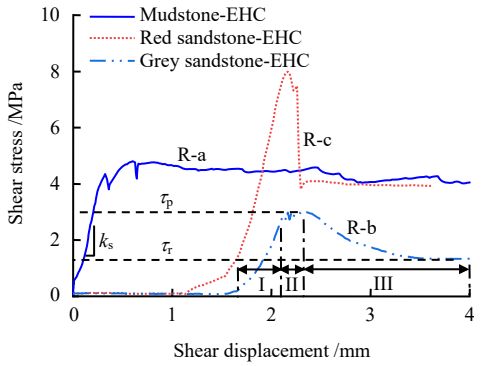



**Fig. 6 Typical shear stress-displacement curve of specimens**

Plastic Deformation Stage (II): In this stage, the partial bonding interface reaches plastic failure, and the stress in the plastic failure zone gradually shifts to the non-plastic failure zone. The shear stiffness decreases progressively until the peak shear strength ($\tau_p$) of the interface is reached.

Plastic Sliding Stage (III): After the $\tau_p$ is reached, the gradual debonding failure of the interface leads to a reduction in the interface's shear strength to the residual strength ($\tau_r$), with the shear resistance ultimately provided solely by the friction at the interface.

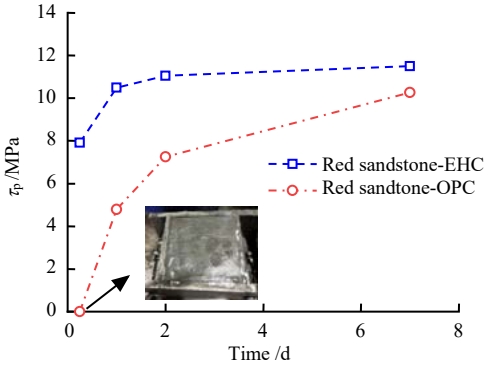
The pre-peak curves of different cement-rock composites are generally consistent. However, the plastic sliding stage (III) can be classified into three types, depending on the interface properties: ideal plastic (R-a in Fig. 6), plastic softening (R-b in Fig. 6), and plastic drop (R-c in Fig. 6). The $k_s$, $\tau_p$, and $\tau_r$ are key indicators that reflect the GRI properties.

### 3.1 Shear strength of GRI

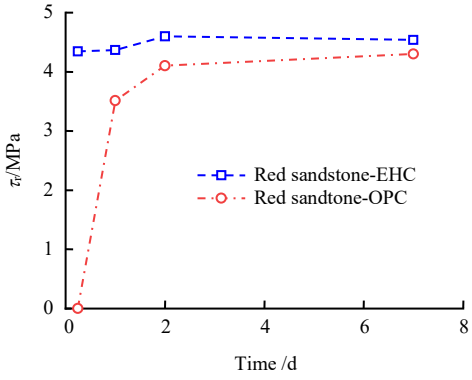
3.1.1 Effect of grout types and curing ages

The peak shear strength $\tau_p$ of the EHC-red sandstone interface at different curing ages is presented in Fig. 7(a).

With the increase of curing time, the $\tau_p$ in EHC conditions increases rapidly, particularly during the early stages of curing. When the curing time increases from 6 hours to 1 day, the $\tau_p$ of EHC bonded specimens increases from 7.9 MPa to 10.5 MPa, representing a 33% increase. However, between 1 day and 7 days of curing, the $\tau_p$ only increases from 10.5 MPa to 11.5 MPa, corresponding to a relatively modest increase of 14.4%. This indicates that the $\tau_p$ of EHC at 1 day can already exceed 90% of its 7-day value, which is sufficient to provide anchorage force to the GRI in a timely manner. In contrast, the OPC bonded specimens exhibit a gradual increase in $\tau_p$. Particularly after 6 hours of curing, OPC has not yet solidified, and the $\tau_p$ at the rock-grout interface is 0. During the curing time from 1 day to 2 days and 7 days, the $\tau_p$ of OPC bonded specimens increases from 4.8 MPa to 7.3 MPa and 10.3 MPa, respectively, representing increases of 52% and 41%. This indicates that the growth rate of $\tau_p$ for OPC also follows a trend of rapid early-stage development and a slower progression in later stages. However, a longer duration is required for $\tau_p$ to stabilize. Under the same conditions, the $\tau_p$ of OPC bonded specimens is significantly lower than that of EHC, but the difference between the two decreases gradually with the increase in curing time. Taking the 1-day age as an example, the $\tau_p$ of EHC and OPC bonded specimens are 10.5 MPa and 4.8 MPa, respectively, with the former being 2.2 times higher than the latter. However, as the curing time increases to 7 days, the $\tau_p$ of EHC is only 12% higher than that of OPC. These results suggest that OPC can also achieve good results in controlling the long-term stability of the anchoring interface.




(a) Peak shear strength




(b) Residual shear strength

**Fig. 7 Shear strength of GRI under different grout types and curing ages**

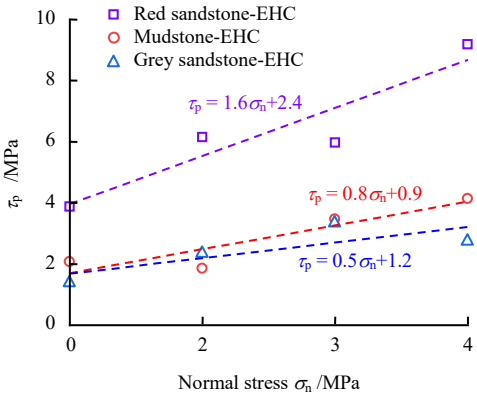
The $\tau_r$ of the EHC-red sandstone interface at different curing times is shown in Fig. 7(b). It can be seen that with the increase of curing time, the $\tau_r$ of both EHC and OPC bond samples gradually increases. In case of EHC, when the curing time increases from 6 hours to 1 day, 2 days, and 7 days, the $\tau_r$ increases from 4.3 MPa to 4.4 MPa, 4.6 MPa, and 4.6 MPa, respectively. The $\tau_r$ in EHC conditions stabilizes within 2 days, with the maximum increase being only 4.4%. In contrast, the $\tau_r$ under OPC conditions increases slowly, but with a noticeable growth. During the curing time from 1 day to 2 days and 7 days, the $\tau_r$ of OPC bonded specimens increases from 3.5 MPa to 4.1 MPa and 4.3 MPa, representing an increase of 17%

and 5%, respectively. It can be observed that the increase in $\tau_r$ for OPC bonded specimens after 2 days is significantly smaller than the increase in $\tau_p$, indicating that the strength improvement of OPC bonded specimens after 2 days is primarily attributed to the development of $\tau_p$. When the curing times are 6 hours, 1 day, 2 days, and 7 days, the $\tau_r/\tau_p$ ratios of EHC are 0.54, 0.42, 0.42, and 0.39, respectively; whereas for OPC at curing times of 1 day, 2 days, and 7 days, the $\tau_r/\tau_p$ ratios are 0.73, 0.57, and 0.45, respectively. With the increase of curing time, the brittle failure characteristics of both interfaces become more pronounced, with EHC showing more significant brittle failure characteristics.

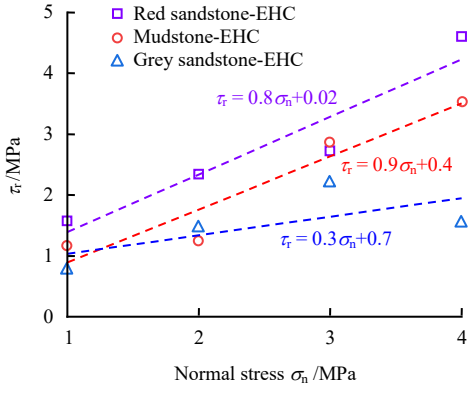
3.1.2 Effect of rock properties

The $\tau_p$ under different rock conditions is shown in Fig. 8(a). Under the same normal stress conditions, the $\tau_p$ of mudstone and grey sandstone are relatively close to each other and are significantly smaller than that of red sandstone. The $\tau_p$ of the three rocks with the EHC bonding interface roughly follows the order: red sandstone > mudstone > grey sandstone. As normal stress increases, the $\tau_p$ of the three rocks increases approximately linearly. According to Mohr-Coulomb theory, the cohesion $c$ and internal friction angle $\varphi$ corresponding to $\tau_p$ are shown in Table 5. The $c$ of mudstone, red sandstone, and grey sandstone are 0.92, 2.39, and 1.17 MPa, respectively, while the $\varphi$ are 38°, 57.6°, and 27°, respectively. It can be observed that red sandstone exhibits higher values of $c$ and $\varphi$ than those of mudstone and grey sandstone, which can be attributed to its greater strength and porosity. For grey sandstone, although its rock strength is comparable to that of red sandstone, its $\tau_p$ is significantly lower. Compared to red sandstone, the reduction in $\varphi$ for grey sandstone is more pronounced than the reduction in $c$, with a decrease of approximately 53%. This is primarily because grey sandstone, being a feldspar-rich sandstone (e.g., potassium feldspar + quartz), has tightly bound mineral particles with smooth surfaces, making it difficult for cement particles to penetrate the rock and form "mechanical interlocking" at the interface, leading to the interface relying mainly on bonding for anchorage strength. For mudstone, the $c$ of GRI decreases by approximately 62% to that of red sandstone conditions, which is more obvious than the decrease of $\varphi$. This is primarily because the clay minerals in mudstone swell upon water absorption, providing pathways for grout particles to penetrate, thereby forming an effective "mechanical interlocking" effect at the interface. As a result, the anchorage strength of the mudstone interface relies mainly on frictional resistance at the interface.

The $\tau_r$ under different rock conditions is shown in Fig. 8(b). Under the same normal stress conditions, the $\tau_r$ of the three rocks with the EHC bonding interface also roughly follows the order: red sandstone > mudstone > grey sandstone. As normal stress increases, the $\tau_r$ of the three rocks increases approximately linearly. The residual cohesion $c_r$ and internal friction angle $\varphi_r$ corresponding to $\tau_r$ are shown in Table 5. The $c_r$ of mudstone, red sandstone, and grey sandstone conditions are 0.02, 0.44, and 0.73 MPa, respectively, while the $\varphi_r$ are 41.1°, 43.5°, and 17.0°, respectively. It can be observed that the $c_r$ of the EHC bonding interface with the three rocks is significantly reduced compared to $c$, with mudstone showing the largest reduction (98%), followed by red sandstone (82%), and grey sandstone (38%). Compared to $\varphi$, the reduction in $\varphi_r$ for red sandstone and grey sandstone is 25% and 37%, respectively, while the $\varphi_r$ for mudstone actually increases by 8%. This further confirms that mudstone and grey sandstone rely on friction and bonding effects to provide shear strength of GRI, respectively. Compared to mudstone, red sandstone has a relatively larger $\varphi_r$, significantly larger than that of grey sandstone. This is primarily due to the higher strength of red sandstone, where the rock and grout fragments filling the cracks after interface failure increase the frictional effect at the interface. Although mudstone fragments can also fill cracks, due to their lower strength, the fragments are more easily crushed during the shearing process, thus resulting in a lower $\varphi_r$ for mudstone than for red sandstone.




(a) Peak shear strength




(b) Residual shear strength

**Fig. 8 Shear strength of the anchorage interface under different rock properties**

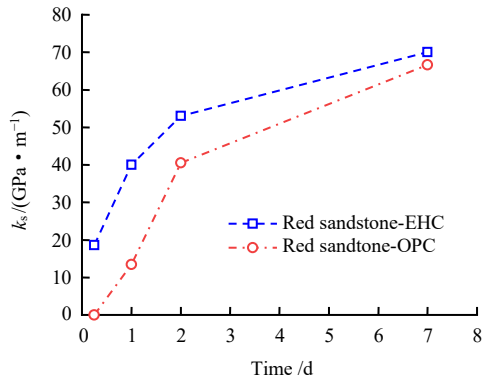
**Table 5 Cohesion strength and internal friction angle of anchorage interface under different rock properties**

| Parameters | $c$ /MPa | $\varphi$ /(°) | $c_r$ /MPa | $\varphi_r$ /(°) |
|---|---|---|---|---|
| Mudstone | 0.920 | 38.0 | 0.02 | 41.11 |
| Red sandstone | 2.385 | 57.6 | 0.44 | 43.45 |
| Grey sandstone | 1.170 | 27.0 | 0.73 | 17.01 |

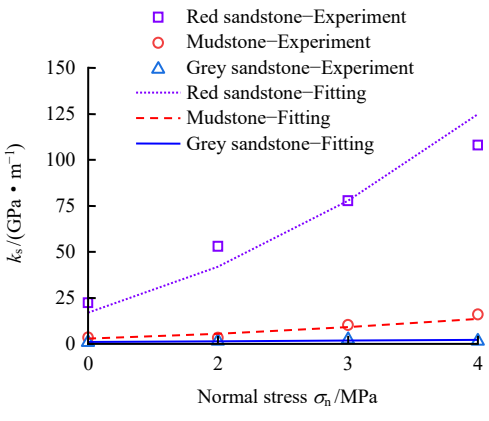
## 3.2 Shear stiffness of GRI

3.2.1 Effect of grout types and curing ages

The shear stiffness $k_s$ of the GRI at different curing ages is presented in Fig. 9(a). With the increase in curing time, the $k_s$ significantly increases. After curing 6 hours, 1 day, 2 days, and 7 days, the $k_s$ of the EHC-red sandstone interface are 16.8 GPa/m, 40 GPa/m, 53 GPa/m, and 70 GPa/m, respectively. After curing 1 day, 2 days, and 7 days, the $k_s$ of the OPC-red sandstone interface are 13.5 GPa/m, 40.5 GPa/m, and 66.6 GPa/m, respectively. It can be observed that the rate of increase of $k_s$ for both OPC and EHC gradually decreases with curing time. Taking the EHC-red sandstone interface as an example, the $k_s$ increased by about 1.8 times from 6 hours to 2 days, but only increased by 1.3 times from 2 days to 7 days. Both types of GRI bonded by OPC and EHC show a significant increase within 2 days, with the increase slowing down after 2 days.




(a) Influence of cement age




(b) Influence of normal stress

**Fig. 9 Shear stiffness of the anchorage interface under different conditions**

3.2.2 Effect of rock properties

The $k_s$ of GRI under different rocks is shown in Fig. 9(b). Under the same normal stress conditions, the $k_s$ between three types of rock and EHC satisfy the order: red sandstone > mudstone > grey sandstone. When the normal stresses are 1, 2, 3, and 4 MPa, the $k_s$ in red sandstone conditions are 22.3, 53, 77.8, and 107.9 GPa/m, respectively; the $k_s$ in mudstone conditions are 3.4, 3.3, 10.15, and 15.9 GPa/m, respectively; the $k_s$ in grey sandstone conditions are 0.8, 1.5, 2.2, and 3 GPa/m, respectively. It can be observed that the $k_s$ increases non-linearly with the increase of normal stress. This is mainly because the increase in normal stress causes the "interlocking" of the interface to become tighter, thereby improving the ability of the interface to resist deformation. The relationship between the $k_s$ and normal stress can be described by follows[41–42]:

$$k_s = Rk_n\left[1-\frac{\sigma_n}{V_m k_n+\sigma_n}\right]^{-2} \tag{2}$$

where $k_n$ is the normal stiffness of the interface; $R$ is the interfacial shear coefficient; and $V_m$ is an independent parameter under initial stress.

It is evident that the response of $k_s$ to normal stress varies significantly among different rocks. When the normal stress increases from 1 MPa to 4 MPa, the increase in $k_s$ for red sandstone, mudstone, and grey sandstone is 383%, 468%, and 375%, respectively. It is evident that $k_s$ in mudstone conditions responds most significantly to normal stress. This may be because the low strength of mudstone allows the grout to permeate more easily, becoming more firmly embedded as normal stress increases, thereby effectively improving the $k_s$. However, grey sandstone, due to its higher strength and denser and smoother interface, has a limited improvement in interlocking effect with increasing normal stress, resulting in the smallest response of $k_s$ to normal stress. The fitting results of $k_s$ are shown in as:

$$\left.\begin{aligned} k_s &= 1.02\left[1-\frac{\sigma_n}{0.45+\sigma_n}\right]^{-2}, \text{ Mudstone-EHC sample}\\ k_s &= 3.15\left[1-\frac{\sigma_n}{0.74+\sigma_n}\right]^{-2}, \text{ Redsandstone-EHC sample}\\ k_s &= 0.78\left[1-\frac{\sigma_n}{1.53+\sigma_n}\right]^{-2}, \text{ sandstone-EHC sample} \end{aligned}\right\} \tag{3}$$

## 3.3 Failure mode of GRI

Due to the significant strength difference between rock and grout, a complex failure mode of the GRI can be observed during the shear process. Shear failure tends to occur preferentially on the side composed of weaker material, where the weak phase may exist in either the rock or the grout component of the specimen. Therefore, it is essential to analyze the shear deformation evolution

of GRI during the shear process. The DIC system, characterized by capturing the micro-displacement of specimens, is employed to quantify full-field displacement and strain evolution during shear testing. A 100 mm× 100 mm observation area centered on the GRI was defined, as shown in Fig. 10, with the origin (0, 0) set at the geometric center of the specimen surface. The horizontal direction is taken as the $u$-direction, and the vertical direction is taken as the $v$-direction. Three critical monitoring points ($P_0$, $P_1$, and $P_2$) are established to represent the horizontal displacement monitoring points of the interface, grout, and rock, respectively. The positions of $P_0$, $P_1$, and $P_2$ are (0, 0), (0, 10), and (0, −10), respectively. The shear deformation of rock and grout near the interface can be expressed as:

$$\left.\begin{aligned}\Delta u_{\mathrm{g}} &= u_{P1} - u_{P0}\\ \Delta u_{\mathrm{r}} &= u_{P2} - u_{P0}\end{aligned}\right\} \tag{4}$$

where $u_{P0}$, $u_{P1}$, and $u_{P2}$ represent the horizontal displacement of interface, grout, and rock, respectively; $\Delta u_{\mathrm{g}}$ and $\Delta u_{\mathrm{r}}$ represent the shear deformation of grout and rock near the interface, respectively.

Based on the relationship between $\Delta u_{\mathrm{g}}$ and $\Delta u_{\mathrm{r}}$, the shear failure of GRI can be classified into three types: (1) When $\Delta u_{\mathrm{g}}>\Delta u_{\mathrm{r}}$, it indicates that the shear deformation of the grout is greater than that of the rock, leading to shear failure of the grout. (2) When $\Delta u_{\mathrm{g}}<\Delta u_{\mathrm{r}}$, it suggests that the shear deformation of the rock is greater than that of the grout, resulting in shear failure of the rock in the sample. (3) When $\Delta u_{\mathrm{g}}=\Delta u_{\mathrm{r}}$, it implies that the shear deformations of both the grout and rock are comparable, leading to interface delamination failure in the sample.

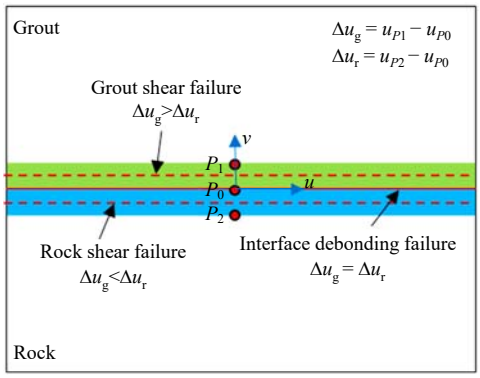
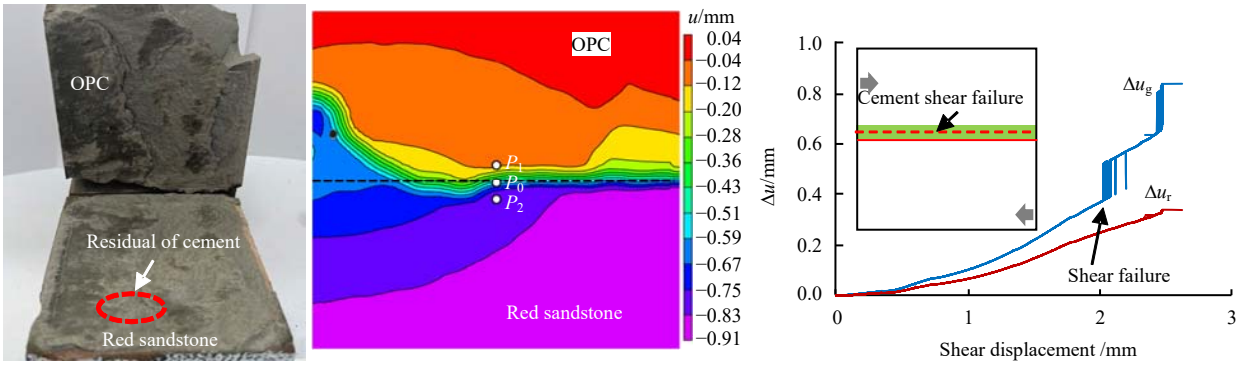


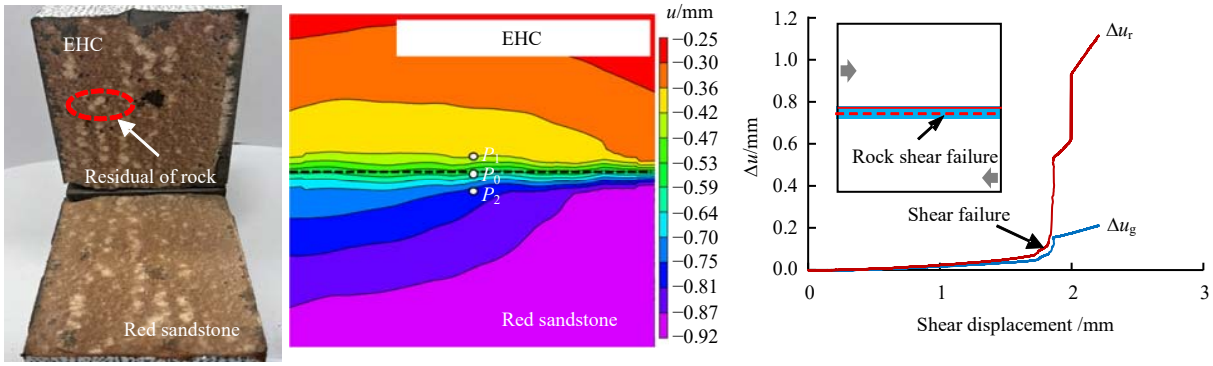

**Fig. 10 Diagram of shear failure at the anchorage interface**

3.3.1 Effect of grout properties

For an age of 1 day, the distribution of horizontal shear displacement at the GRI of red sandstone under different grout materials is shown in Fig. 11.




(a) OPC




(b) EHC

**Fig. 11 Failure modes of the anchorage interface with different grouting materials (the left figure is a horizontal displacement cloud image, and the right figure is the displacement difference of the data extraction point)**

As depicted in Fig. 11(a), when bonding with OPC, the shear deformation of the specimen is mainly concentrated on the grout side, while the shear deformation on the rock side is relatively smaller. The horizontal displacement contour map also shows that the specimen exhibits significant shear deformation near the interface, with a tendency for shear deformation to propagate through the grout. This suggests that the strength of the grout is lower than that of the rock, and the propagation of shear cracks within the grout and at the interface is the fundamental cause of shear failure in the specimen. During shear loading, out-of-plane deformation occurs at the load boundaries, leading to localized material detachment, which may compromise the accuracy of displacement measurements in those regions. Nevertheless, quantitative analysis indicates that these boundary effects are minimal and confined to small, localized zones. By extracting the displacement data from monitoring points during shear, it can be seen that $\Delta u_g$ is always greater than $\Delta u_r$, and the difference between them increases gradually with the horizontal displacement. When the shear stress reaches $\tau_p$, a sudden increase in $\Delta u_g$ leads to shear failure along the grout, and a distinct layer of residual grouting is observed on the rock surface after failure. This indicates that in the case of OPC, the strength of the grout increases slowly, making it susceptible to grout failure.

As shown in Fig. 11(b), when bonding with EHC, the shear deformation of the specimen is primarily concentrated near the interface, with the deformation regions on both the grout and rock sides being symmetrically distributed. By extracting displacement data from monitoring points during shear, it can be seen that before the shear stress reaches $\tau_p$, both $\Delta u_g$ and $\Delta u_r$ increase slowly with the shear stress, and the difference between them is not significant. When the shear stress reaches $\tau_p$, the sudden increase in $\Delta u_r$ results in shear failure of rock, and a distinct layer of residual rock is observed on the grout surface after failure. This indicates that EHC exhibits rapid strength growth characteristics (with UCS reaching 70 MPa after curing for 1 day), enabling tight bonding with the rock during the early stage. At this point, the strength of the rock becomes the key factor controlling GRI performance. Notably, compared to OPC, the failure surface of the EHC-bonded specimen is relatively smooth. This is because the $\Delta u$ values between the grout and the rock before failure are small, reducing the initiation and development of internal cracks, leading to a smoother shear failure surface in the specimen.

3.3.2 Effect of rock properties

Taking the example of a normal stress of 1 MPa, the distribution of shear displacement for various rocks and EHC-bonded specimens is shown in Fig. 12.

As shown in Fig. 12(a), under the mudstone condition, the shear deformation of the specimen is primarily concentrated in the rock near the interface, while the shear deformation in the grout is relatively small. By extracting displacement data from the monitored points during the shear process, it is evident that before the shear stress reaches $\tau_p$, both $\Delta u_g$ and $\Delta u_r$ increase slowly with increasing shear stress, and the difference between them is not significant. However, when the shear stress reaches $\tau_p$, there is a sudden increase in $\Delta u_r$, and shear failure occurs along the rock. After failure, a clear layer of rock residue is visible on the surface of the grout. In comparison to the red sandstone specimens, the mudstone specimens exhibit a significantly thicker layer of mudstone residue on the surface of the grout after failure. This is due to the relatively low strength of mudstone and its susceptibility to water absorption and softening, which leads to a significant degradation of strength near the interface, causing more pronounced failure characteristics in the mudstone specimens.

As shown in Fig. 12(b) and Fig. 12(c), as the rock strength increases, the shear deformation of the specimen gradually shrinks to near the interface. By extracting displacement data from the monitored points during the shear process, it can be observed that before the shear stress reaches $\tau_p$, the difference between $\Delta u_g$ and $\Delta u_r$ decreases and increases slowly. However, when the shear stress reaches $\tau_p$, a sudden increase in $\Delta u_r$ causes shear failure along the rock. Unlike mudstone, the rough surface of red sandstone has a better "interlocking" effect with the grout, which results in a significantly smaller shear deformation required to reach $\tau_p$ compared to mudstone. For the grey sandstone specimen, whether before or after the shear stress reaches $\tau_p$, both $\Delta u_g$ and $\Delta u_r$ increase slowly with increasing shear deformation, without exhibiting any significant sudden increase, and the difference between $\Delta u_g$ and $\Delta u_r$ is small. This indicates that the grey sandstone specimen primarily undergoes interface debonding failure, and the rock surface remains smooth after failure, with no residual grouting layer.

## 4 Discussion

### 4.1 Relation of shear strength parameters between GRI and rock and grout

The shear strength of the GRI is closely related to the properties of rock and grout, and the effects of rock and grout on the shear strength of the GRI can be expressed as:

$$\left.\begin{aligned} \eta_{c_g} &= \frac{c_p}{c_{p_g}}, \eta_{c_r} = \frac{c_p}{c_{p_r}} \\ \eta_{\varphi_g} &= \frac{\varphi_p}{\varphi_{p_g}}, \eta_{\varphi_r} = \frac{\varphi_p}{\varphi_{p_r}} \end{aligned}\right\} \tag{5}$$

where $c_p$ and $\varphi_p$ are the cohesion and internal friction angle of the interface, respectively; $\eta_{c_g}$ and $\eta_{\varphi_g}$ are the impact factors of cohesion and internal friction angle of hardened grout, respectively; $\eta_{c_r}$ and $\eta_{\varphi_r}$

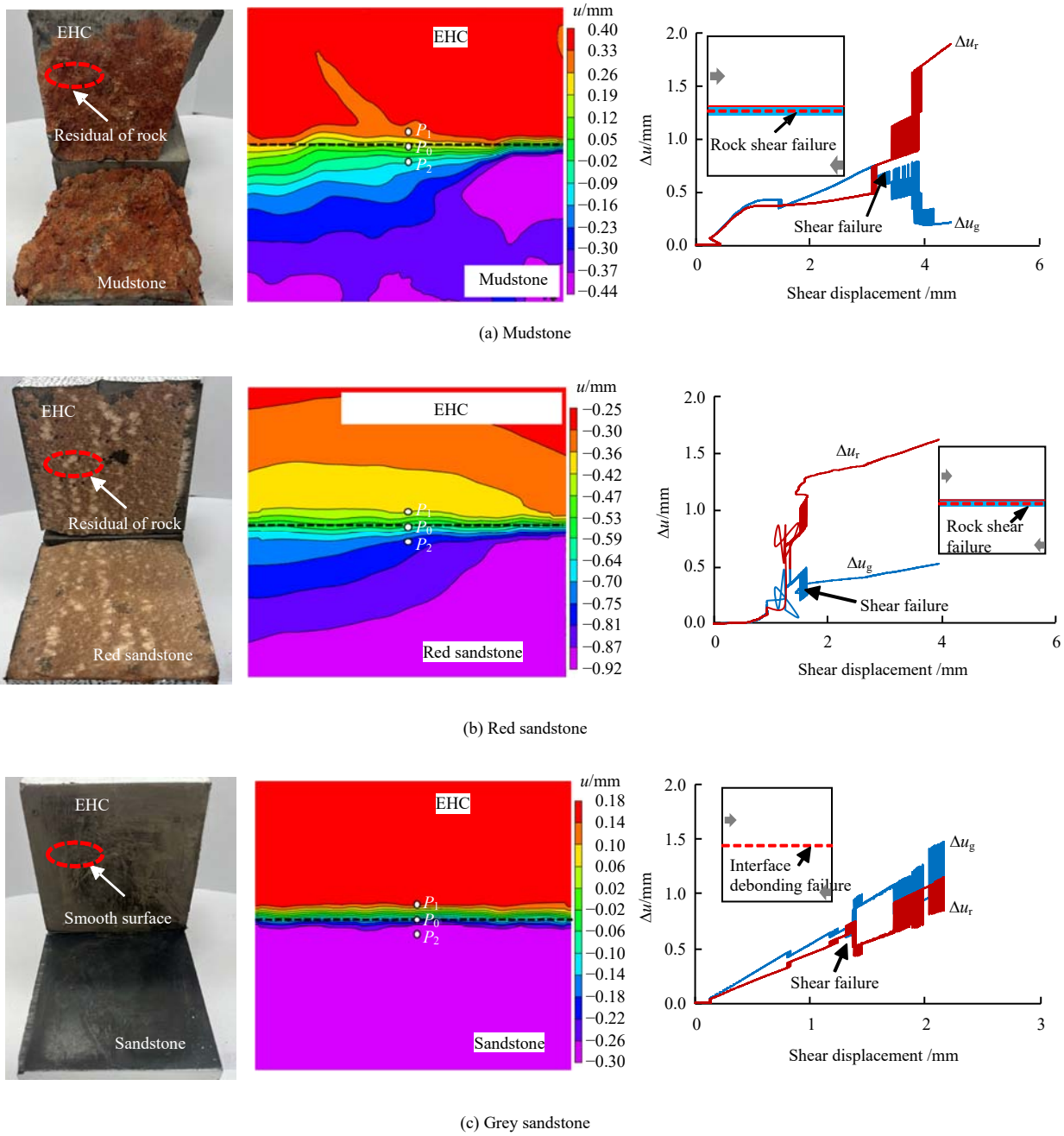


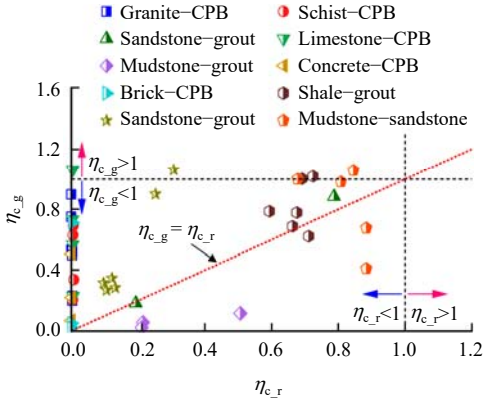

**Fig. 12 Failure modes of different rock anchorage interfaces**

are the impact factors of cohesion and internal friction angle of rock, respectively; $c_{p_g}$ and $\varphi_{p_g}$ are the cohesion and internal friction angle of hardened grout, respectively; and $c_{p_r}$ and $\varphi_{p_r}$ are the cohesion and internal friction angle of rock, respectively.

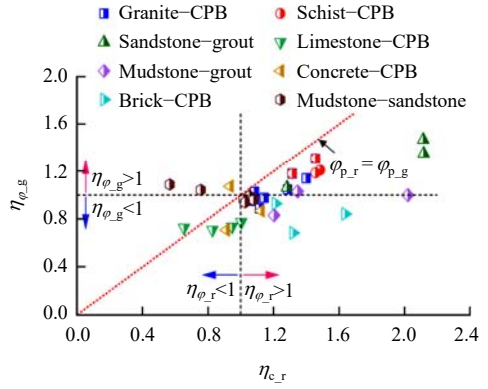
Suppose the ratio of the GRI and rock shear strength parameters is taken as the horizontal axis, and the ratio of the GRI and hardened grout as the vertical axis. In that case, the variation of the shear strength parameters under different rock and grout conditions is shown in Fig. 13. Taking the cohesion as an example, as shown in Fig. 13(a), if $\eta_{c_g} > \eta_{c_r}$, it indicates that the cohesion of GRI is closer to that of the hardened grout, and the properties of the grout primarily influence the GRI. Conversely, it is mainly influenced by the properties of the rock. This law is also applicable to the internal friction angle of GRI. By reviewing relevant literature [4, 6, 18, 43−45], the relationship between the shear strength ratio of different types of red bed rock and grout is summarized, as shown in Fig. 13.

It can be seen from Fig. 13(a) that most of the $\eta_{c_g}$ are larger than $\eta_{c_r}$, indicating that the properties of the grout primarily influence the cohesion of GRI. Only some of the mudstone-grout interface, schist-CPB interface, and shale-grout interface show the opposite trend. Furthermore, most of $\eta_{c_g}$ and $\eta_{c_r}$ are less than 1, indicating that most of the cohesion of GRI is less than that of rock and grout. From Fig. 13(b), it can be seen that most of the $\eta_{\varphi_g}$ are smaller than $\eta_{\varphi_r}$, indicating that the properties of the rock primarily influence the

internal friction angle of GRI. In case of the Brick-CPB interface and mudstone-grout interface, the $\eta_{\varphi_g}$ is less than 1, but the $\eta_{\varphi_r}$ is greater than 1, indicating that the internal friction angle of GRI lies between the rock and grout. In case of schist and granite-CPB interface and sandstone-grout interface, the $\eta_{\varphi_g}$ and $\eta_{\varphi_r}$ are both greater than 1, suggesting that the internal friction angle of GRI exceeds those of both the rock and the grout.




(a) Cohesion




(b) Internal friction angle

**Fig. 13 Relation of shear strength ratio under different rock and grout types[4, 6, 18, 43−45]**

It can be seen that the shear behavior of GRI is related to the properties of rock and grout. The shear resistance of the GRI is mainly governed by the weaker material (rock or grout). A significant enhancement in the shear strength of GRI occurs only when the strength ratio between the grout and the rock falls within a specific range. For mudstone with lower strength and high hydro-sensitivity, the "water-rock" interactions will soften the mudstone and weaken the bonding effect of GRI. In this case, the bonding strength of GRI is extremely limited, and the friction strength becomes the main component of shear strength. For sandstone with higher strength but a smooth surface, the ITZ with a biphasic membrane will be formed due to the oversaturation reactions of $Ca(OH)_2$. The ITZ exhibits higher porosity and inferior mechanical properties, making it a vulnerable zone where GRI damage tends to occur (Li et al.[22]). Therefore, the shear strength of GRI is mainly influenced by the rock strength, rock surface roughness, grout strength, the mechanical parameter of ITZ, and normal stress. It is urgent to propose a novel shear strength model to predict the anchorage stability.

### 4.2 Shear strength models of GRI

The $\tau_p$ of the GRI is mainly composed of two parts: the interface friction strength and the bonding strength[46], as shown in Eq. (6).

$$\tau_p = \tau_{JRC} + \tau_c \tag{6}$$

where $\tau_{JRC}$ and $\tau_c$ are the friction strength and bonding strength of GRI, respectively.

(1) Friction strength $\tau_{JRC}$

Through direct shear tests on jointed rock masses, a novel parameter, the joint roughness coefficient (JRC), has been proposed to quantitatively characterize the roughness of interfaces[47−48]. On this basis, a shear strength criterion for joint surfaces has been developed:

$$\tau_{JRC} = \sigma_n \tan\left[\mathrm{JRC}\lg\left(\frac{\mathrm{JCS}}{\sigma_n}\right)+\varphi_b\right] \tag{7}$$

where JRC is the joint roughness coefficient; JCS is the compression strength of the joint wall (MPa); and $\varphi_b$ is the basic friction angle (°).

For GRIs composed of different materials on both sides, the parameters JCS[13] and $\varphi_b$[49] need to be modified, as shown

$$\left.\begin{aligned}&\mathrm{JCS_i} = a\times\mathrm{JCS_r}+(1-K)\times\mathrm{JCS_g}\\&a=\frac{\mathrm{JCS_r}}{\mathrm{JCS_r}+\mathrm{JCS_g}}\end{aligned}\right\} \tag{8}$$

$$\varphi_b^i = 0.981\,5\varphi_b^w + 0.053\,7\varphi_b^s \tag{9}$$

where $\mathrm{JCS_i}$, $\mathrm{JCS_r}$ and $\mathrm{JCS_g}$ represent the compressive strengths of interface, rock and grout, respectively (MPa); $\varphi_b^i$ is the basic friction angle of the interface $\varphi_b^w$ and $\varphi_b^s$ represent the basic friction angles of the weaker and stronger materials on either side of the GRI, respectively. In the absence of experimental data, the basic friction angle can be substituted with the residual friction angle of the material[47].

(2) Bonding strength $\tau_c$

The bonding strength $\tau_c$ can be represented by the integral of the bonding unit over the bonding area, as shown in Eq. (10)[49]:

$$\tau_c = \frac{\iint_S c_m \mathrm{d}S}{A} \tag{10}$$

where $S$ is the bonding area of the interface; and $A$ is a plane stereoscopic projection on the interface (mm²).

The bonding strength $c_m$ of the bonding unit isclosely related to the micromechanical properties of the grout-rock interface, which can be expressed as[50]:

$$c_{\mathrm{m}}=\frac{\sqrt{3}}{9}H_{\mathrm{ITZ}} \tag{11}$$

where $H_{\mathrm{ITZ}}$ is the microscopic hardness of ITZ.

The microscopic hardness of the sample is generally tested using the nanoindentation method. Before testing, the sample, which includes the GRI, is cut into small pieces of 10 mm×10 mm×10 mm. The testing surface of the sample is then finely polished, followed by nanoindentation tests on the polished surface to obtain the micro-mechanical characteristics of the sample's surface. Due to the high surface flatness required for nanoindentation, polishing of the sample surface typically takes 1−2 weeks, making it difficult to test samples at 6 hours, 1 day, 2 days, and 7 days as in this study. Research has shown[20] that the micro-mechanical parameters of the sample are closely related to porosity, and the relationship between micro-hardness and porosity is given by Eq. (10). Therefore, the porosity of OPC and EHC under different curing periods was tested, and the results are shown in Fig. 11. As the curing age increases, the porosity of both OPC and EHC decreases gradually. The experiment shows[22] that after 28 days, the $H_{\mathrm{ITZ}}$ of OPC and EHC are 23.8 GPa and 30 GPa, respectively, with porosities of 20% and 17.2%, respectively. Substituting these values into Eq. (10), the $H_0$ of OPC and EHC can be obtained.

$$H_{\mathrm{ITZ}}=H_0\times(1-p)^2 \tag{12}$$

where $p$ is the volume fraction of spherical pores; and $H_0$ is the microhardness of the material after its properties have stabilized.

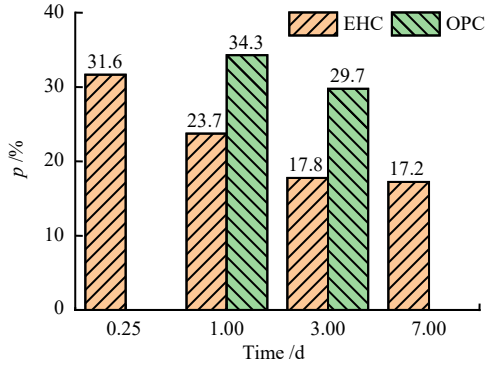



**Fig. 14 Porosity of EHC and OPC at different curing times**

Due to the heterogeneity in the porosity distribution, the GRI is prone to progressive failure from high porosity regions to low porosity regions at the microstructural level. Assuming that the ITZ is homogeneous, the $\tau_c$ can be expressed as

$$\tau_{\mathrm{c}}=\frac{\sqrt{3}}{9}\eta\times H_0\times(1-p)^2 \tag{13}$$

where $\eta$ is the coefficient of porosity heterogeneity.

Cambining equations (7), (8), (9) and (13), $\tau_{\mathrm{p}}$ of the GRI can be expressed as

$$\tau_{\mathrm{p}}=\sigma_{\mathrm{n}}\tan\left[\mathrm{JRC}\times\lg\left(\frac{a\times\mathrm{JCS_r}+(1-a)\times\mathrm{JCS_g}}{\sigma_{\mathrm{n}}}\right)+0.981\,5\varphi_{\mathrm{b}}^{\mathrm{w}}+0.053\,7\varphi_{\mathrm{b}}^{\mathrm{s}}\right]+\frac{\sqrt{3}}{9}\eta\times H_0\times(1-p)^2 \tag{14}$$

According to references[51−54], the GRI parameters for red sandstone, mudstone, grey sandstone, OPC, and EHC are shown in Table 6. The fitted results and comparison with experimental data are presented in Table 6 and Fig. 15. It can be observed that Equation (14) can effectively predict the shear strength of the GRI under various conditions, with the error between the experimental and predicted values generally controlled within 20%.

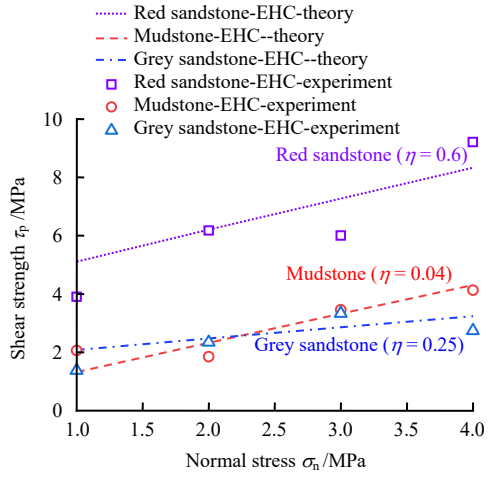
When bonding with EHC, the $\eta$ for red sandstone, mudstone, and grey sandstone are 0.60, 0.04, and 0.25, respectively, and the fitting results are shown in Fig. 15(a). To verify the general applicability of the obtained $\eta$, the same $\eta$ is used to predict the $\tau_{\mathrm{p}}$ of GRI at different curing times. The fitting results are shown in Fig. 15(b). The obtained $\eta$ in Eq. (14) is closely related to the rock properties, with little correlation to the grout properties. Therefore, it is evident that the $\eta$ of red sandstone, mudstone, and grey sandstone can be taken as 0.60, 0.04, and 0.25, respectively. In the absence of experimental data for GRI shear strength, Eq. (12) can be used to estimate the interface shear strength. This provides a useful tool for the rapid evaluation of anchorage strength in red bed tunnels.

This study has several limitations that should be acknowledged: (1) the influence of groundwater on the shear behavior of GRI was not considered, despite its

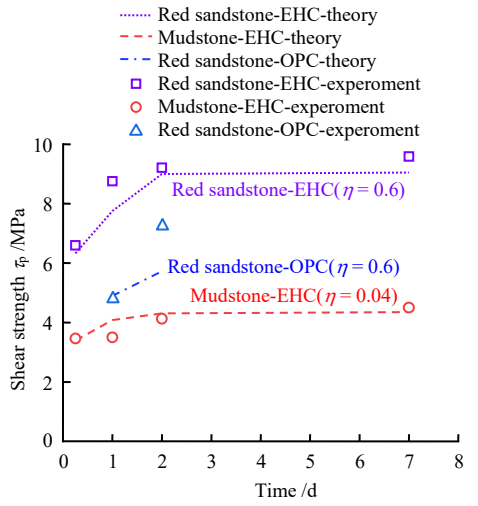
**Table 6 Comparative of predicted and experimental shear strength of gout-rock interface**

| Cement | Rock | Time /d | $p$ | $\sigma_{\mathrm{n}}$ /MPa | JRC | $\mathrm{JCS_r}$ /MPa | $\mathrm{JCS_g}$ /MPa | $\varphi_{\mathrm{b}}^{\mathrm{w}}$ /(°) | $\varphi_{\mathrm{b}}^{\mathrm{s}}$ /(°) | $H_0$ /GPa | $\eta$ | $\tau_{\mathrm{p1}}$ /MPa | $\tau_{\mathrm{p2}}$ /MPa | Error /% |
|---|---|---|---|---|---|---|---|---|---|---|---|---|---|---|
| EHC | RS | 2.00 | 0.18 | 4 | 2 | 24.0 | 75.0 | 43.5 | 45 | 50 | 0.60 | 8.3 | 9.2 | 9.8 |
| EHC | M | 2.00 | 0.18 | 4 | 2 | 2.7 | 75.0 | 41.1 | 45 | 50 | 0.04 | 4.3 | 4.1 | 4.9 |
| EHC | GS | 2.00 | 0.18 | 4 | 2 | 8.2 | 75.0 | 17.0 | 45 | 50 | 0.25 | 3.2 | 2.7 | 18.5 |
| EHC | RS | 0.25 | 0.32 | 4 | 2 | 24.0 | 53.1 | 43.5 | 35 | 50 | 0.60 | 5.9 | 6.6 | 10.6 |
| EHC | RS | 1.00 | 0.24 | 4 | 2 | 24.0 | 73.5 | 43.5 | 40 | 50 | 0.60 | 7.2 | 8.6 | 16.3 |
| EHC | RS | 7.00 | 0.17 | 4 | 2 | 24.0 | 79.9 | 43.5 | 50 | 50 | 0.60 | 8.4 | 9.6 | 12.5 |
| OPC | RS | 1.00 | 0.34 | 4 | 2 | 24.0 | 10.0 | 43.5 | 35 | 35 | 0.60 | 4.9 | 4.8 | 2.1 |
| OPC | RS | 2.00 | 0.30 | 4 | 2 | 24.0 | 32.0 | 43.5 | 45 | 35 | 0.60 | 5.7 | 7.3 | 21.9 |
| EHC | M | 1.00 | 0.24 | 4 | 2 | 2.7 | 73.5 | 41.1 | 40 | 50 | 0.04 | 4.0 | 3.5 | 14.3 |
| EHC | M | 7.00 | 0.17 | 4 | 2 | 2.7 | 79.9 | 41.1 | 50 | 50 | 0.04 | 4.4 | 4.5 | 2.2 |

Note: RS, M, and GS represent red sandstone, mudstone, and grey sandstone, respectively; $\tau_{\mathrm{p1}}$ and $\tau_{\mathrm{p2}}$ represent the experimental and predicted shear strengths of GRI, respectively.




(a) Impact of normal stress




(b) Impact of curing time

**Fig. 15 Comparative of predicted and experimental shear strength of the gout-rock interface**

potential to alter the mineral composition and mechanical properties of red beds; (2) the empirical model was validated exclusively for cement-based grouts, which raises uncertainty regarding its applicability to other bonding materials (e.g., polymer resins); (3) the effects of high surface roughness and varying normal stress levels on shear failure mechanisms were not comprehensively investigated. Future studies should address these aspects to enhance the model's applicability in practical engineering scenarios.

## 5 Conclusions

Based on direct shear test and DIC technology, this study innovatively investigates the shear mechanical properties of the GRI between three typical red beds soft rocks (red sandstone, mudstone, and grey sandstone) and two typical grout materials (OPC and EHC) under different curing periods (6 h, 1 d, 2 d, 7 d). The shear behavior and DIC-based failure mode are analyzed for red beds GRIs, and the relationships among the shear strength of the interface, rock, and grout are thoroughly investigated. The main conclusions are as follows:

(1) In red beds, the GRI shear strength $\tau_p$ of the GRI follows the order: red sandstone > mudstone > grey sandstone. The grey sandstone and mudstone exhibit smooth surfaces and low strengths, respectively, which contribute to poor bonding with grout. As the curing age increases, both $\tau_p$ and $k_s$ of the GRI increase non-linearly. Compared with OPC, EHC exhibits better $\tau_p$ and $k_s$, especially for early curing. The $\tau_p$ of the EHC-rock interface after 2 days of curing can reach 90% of the 7-day value. In contrast to $\tau_p$, the $k_s$ of GRI increases more slowly with curing age.

(2) The shear failure characteristics of GRI are related to rock and grout properties. Compared to EHC, when bonded with OPC, grout failure is more likely to occur due to greater shear deformation of the grout relative to the rock during shearing. When bonding with EHC, rock failure easily occurs with the shear deformation of the rock greater than that of the grout. For grey sandstone, the shear deformation of the rock is comparable to that of the grout, and the primary failure mode is debonding.

(3) The shear behavior of GRI is significantly influenced by the rock strength, interface roughness, grout strength, and microstructure of ITZ. Both low-strength rock and grout can cause the sample to fail along the weaker material, leading to reduced bonding strength. For high-strength rock and grout, the porosity of ITZ plays a vital role and exhibits a negative relation with the bonding strength of GRI due to reduced microhardness. An empirical model is developed and validated to estimate the shear strength of the GRI in red bed soft rocks, offering a practical framework for the rapid and reliable assessment of anchorage performance in red bed tunnels.

## Reference

[1] TIAN Y, CHEN W Z, TIAN H M, et al. Physical model test and application of 3D printing rock-like specimens to laminated rock tunnels[J]. Journal of Rock Mechanics and Geotechnical Engineering, 2024, 16(11): 4625−4637.

[2] CHEN X J, ZHANG J Z, HU Y, et al. Random large-deformation modelling on face stability considering dynamic excavation process during tunnelling through spatially variable soils[J]. Canadian Geotechnical Journal, 2025, 62: 1−21.

[3] CHEN X J, LIU L, REN S P, et al. Physical modelling of face stability and ground settlement in EPB shield tunnelling incorporating dynamic cutterhead–soil interaction[J]. Tunnelling and Underground Space Technology, 2026, 170: 107332.

[4] KOUPOULI N J F, BELEM T, RIVARD P. Shear strength between cemented paste backfill and natural rock surface replicas[C]//Proceedings of the First International Conference on Underground Mining Technology. Perth: [s. n.], 2017.

[5] KOUPOULI N, TIKOU B, EFFENGUET H. Direct shear tests on cemented paste backfill-rock wall and cemented paste backfill-backfill interfaces[J]. Journal of Rock Mechanics

and Geotechnical Engineering, 2016, 8(4): 472−479.

[6] YANG R W, HE S, LIU J Y, et al. Tensile strength and failure mechanism of rock–cement sample: roles of curing temperature, nano-silica and rock type[J]. Cement and Concrete Research, 2024, 186: 107673.

[7] XU Jing-mao, GU Lei-yu. Testing study on the peak shear strength between grout and bore wall in the interior bond section of prestressed anchorage cable[J]. Chinese Journal of Rock Mechanics and Engineering, 2004, 23(22): 3765−3769.

[8] LIU Chang-wu, LU Shi-liang. Effects of cement grouting reinforcement on engineering rock masses[J]. Journal of China University of Mining and Technology, 2000, 29(5): 12−16.

[9] SHEN Yan-jun, WEI Xin, YANG Geng-she, et al. Freeze–thaw deterioration model and experimental analysis of rock–concrete interface bonding strength[J]. Chinese Journal of Rock Mechanics and Engineering, 2020, 39(3): 480−490.

[10] WANG Bao-tian, ZHANG Fu-hai, ZHANG Wen-hui. Experimental study on shear strength of granite–concrete bonded interface[J]. Rock and Soil Mechanics, 2004, 25(11): 1717−1721.

[11] SHEN Y, WANG Y, YANG Y, et al. Influence of surface roughness and hydrophilicity on bonding strength of concrete-rock interface[J]. Construction and Building Materials, 2019, 213: 156−166.

[12] Standardization Administration of the People's Republic of China. GB/T 17671—2020 Test method of cement mortar strength (ISO method)[S]. Beijing: Standards Press of China, 2020.

[13] WU Q, XU Y J, TANG H M, et al. Peak shear strength prediction for discontinuities between two different rock types using a neural network approach[J]. Bulletin of Engineering Geology and the Environment, 2019, 78(4): 2315−2329.

[14] GU X L, HONG L, WANG Z L, et al. Experimental study and application of mechanical properties for the interface between cobblestone aggregate and mortar in concrete[J]. Construction and Building Materials, 2013, 46: 156−166.

[15] QIU X, CHEN W Z, YUAN J Q, et al. Study on early hydration and mechanical properties of ferrite-rich calcium sulfoaluminate cement-based grouting materials[J]. Construction and Building Materials, 2024, 411: 134324.

[16] QIU X, CHEN W Z, YUAN J Q, et al. Long-term performance of ferrite-rich calcium sulfoaluminate cement- based paste under seawater corrosion[J]. Construction and Building Materials, 2023, 377: 131056.

[17] QIU X, YUAN J Q, CHEN W Z, et al. Effect of chloride binding and sulfate ion attack on the chloride diffusion in calcium sulfoaluminate-based material under seawater environment[J]. Journal of Materials Research and Technology, 2024, 30: 4261−4271.

[18] NASIR O, FALL M. Shear behaviour of cemented pastefill-rock interfaces[J]. Engineering Geology, 2008, 101(3): 146−153.

[19] LU Yin-long, HE Meng-qi, LI Wen-shuai, et al. Micromechanical mechanism of grouting reinforcement for rock structural planes and optimization of grout–rock bonding interface structure[J]. Chinese Journal of Rock Mechanics and Engineering, 2020, 39(9): 1808−1818.

[20] XIE Y, CORR D J, JIN F, et al. Experimental study of the interfacial transition zone (ITZ) of model rock-filled concrete (RFC)[J]. Cement and Concrete Composites, 2015, 55: 223−231.

[21] BARNES B D, DIAMOND S, DOLCH W L. The contact zone between portland cement paste and glass "aggregate" surfaces[J]. Cement and Concrete Research, 1978, 8(2): 233−243.

[22] LI Wen-shuai, JIANG Bang-you, GU Shi-tan, et al. Experimental study on the shear behavior of grout-infilled specimens and micromechanical properties of grout-rock interface[J]. Journal of Central South University, 2022, 29(5): 1686−1700.

[23] LIU P, XIE S S, LIU L, et al. Experimental study on bonding strength between high-strength bolt and cement-based grouting material[J]. Journal of Materials Research and Technology, 2022, 19: 2191−2203.

[24] WANG W C, DUONG H T H, ZHANG C H. Influence of accelerating admixtures on high early strength cement performance using heat curing method[J]. Case Studies in Construction Materials, 2022: e01746.

[25] LIANG R, LIU Q, HOU D S, et al. Flexural strength enhancement of cement paste through monomer incorporation and in situ bond formation[J]. Cement and Concrete Research, 2022, 152: 106675.

[26] CAI X H, YANG D, ZHANG D, et al. Development of high-early-strength low-carbon engineered cementitious composites with calcium sulfoaluminate cement incorporating high-volume fly ash[J]. Case Studies in Construction Materials, 2023, 18: e01959.

[27] ABDULRAHMAN P I, BZENI D K. Bond strength evaluation of polymer modified cement mortar incorporated with polypropylene fibers[J]. Case Studies in Construction Materials, 2022, 17: e01387.

[28] WANG H H, YANG J, SUN Y H, et al. Experimental investigation of the shear bond strength between HGM cement and shallow formation in deepwater environments[J]. Geoenergy Science and Engineering, 2023, 221: 111174.

[29] ONUAGULUCHI O, RATU R, BANTHIA N. Effect of sodium sulfate activation on the early-age matrix strength and steel fiber bond in high volume fly ash (HVFA) cement mortar[J]. Construction and Building Materials, 2022, 341: 127808.

[30] CHAI L J, YUE Z H, GUO L P, et al. Mechanical constitutive behavior and microstructure evolution of high ductility concrete rapid repair material at different curing ages[J]. Construction and Building Materials, 2025, 458: 139600.

[31] HE X, WEI L, YANG K, et al. Effects of curing temperature and age on the mechanical properties and damage law of coal-based solid waste cemented backfill[J]. Case Studies in Construction Materials, 2025, 23: e04937.

[32] OSMAN H, MOHD HASAN M R, XIN T W L, et al. Effects of bonding enhancers on shear stress and bonding strength of modified asphalt binders under different aging and moisture conditions[J]. Construction and Building Materials, 2024,

453: 139020.

[33] ZHANG C, WANG J, SONG W D, et al. Study on shear behavior and microstructure of rock and cemented paste backfill interface[J]. Construction and Building Materials, 2024, 443: 137834.

[34] DING R H, ZHANG Y F, ZHAO Y, et al. Experimental investigation on fractal mechanism and shear failure characteristics of cement mortar at different curing ages[J]. Journal of Building Engineering, 2024, 93: 109851.

[35] XUE C F, HUANG H, CHEN A, et al. Experimental study and theoretical calculation of age-dependent shear performance of MPCC-NC interface[J]. Case Studies in Construction Materials, 2025, 22: e04887.

[36] LIAO C, LIN B H, LI M, et al. Study on the properties of graphene oxide cementitious grout materials and its cementing effect in reinforcing broken rock mass by grouting[J]. Journal of Building Engineering, 2024, 96: 110458.

[37] LIANG Jiong-jun. Manual of anchoring and grouting technology[M]. Beijing: China Electric Power Press, 1999.

[38] WANG Yun-fei, MA Yong-chao, LI Zhi-chao, et al. Experimental study on shear energy storage and maximum shear strain characteristics of red sandstone[J]. Engineering Mechanics, 2023, 40(2): 66−73.

[39] JIANG W J, QIN M K, WANG W K, et al. Genesis of gray sandstone within the red beds in HLJ-DL uranium deposit, southwest Songliao Basin and its relationship with uranium mineralization[J]. Ore Geology Reviews, 2024, 168: 106035.

[40] CHEN Y D, YU Q J, ZHU Q Z. Experimental investigation and micromechanics-based damage modeling of the stress relaxation mechanical properties in gray sandstone[J]. Computers and Geotechnics, 2022, 149: 104829.

[41] TANG Yong, SUN Zhi-hui. Study on excavation stability of layered soft rock tunnels and asymmetric bolt support method[J]. Journal of Chongqing Jiaotong University (Natural Science Edition), 2020, 39(4): 52−60.

[42] TANG Ya-ming. Study on risk assessment and monitoring–early warning technology of loess landslides in northern Shaanxi[D]. Beijing: China University of Geosciences (Beijing), 2012.

[43] KOUPOULI N J F, BELEM T, RIVARD P, et al. Direct shear tests on cemented paste backfill–rock wall and cemented paste backfill–backfill interfaces[J]. Journal of Rock Mechanics and Geotechnical Engineering, 2016, 8(4): 472−479.

[44] FALL M, NASIR O. Mechanical behaviour of the interface between cemented tailings backfill and retaining structures under shear loads[J]. Geotechnical and Geological Engineering, 2010, 28(6): 779−790.

[45] WU Qiong, WANG Xiao-han, TANG Hui-ming, et al. Shear property and water-induced deterioration of discontinuities between different types of rocks in Badong formation[J]. Rock and Soil Mechanics, 2019, 40(5): 1881−1889, 1897.

[46] MOUZANNAR H, BOST M, LEROUX M, et al. Experimental study of the shear strength of bonded concrete–rock interfaces: surface morphology and scale effect[J]. Rock Mechanics and Rock Engineering, 2017, 50(10): 2601−2625.

[47] BARTON N, CHOUBEY V. The shear strength of rock joints in theory and practice[J]. Rock Mechanics, 1977, 10(1): 1−54.

[48] BARTON N. Review of a new shear-strength criterion for rock joints[J]. Engineering Geology, 1973, 7(4): 287−332.

[49] MORADIAN Z A, BALLIVY G, RIVARD P. Application of acoustic emission for monitoring shear behavior of bonded concrete–rock joints under direct shear test[J]. Canadian Journal of Civil Engineering, 2012, 39(8): 887−896.

[50] NIX W D, GAO H. Indentation size effects in crystalline materials: a law for strain gradient plasticity[J]. Journal of the Mechanics and Physics of Solids, 1998, 46(3): 411−425.

[51] ALEJANO L R, GONZÁLEZ J, MURALHA J. Comparison of different techniques of tilt testing and basic friction angle variability assessment[J]. Rock Mechanics and Rock Engineering, 2012, 45(6): 1023−1035.

[52] JANG H S, ZHANG Q Z, KANG S S, et al. Determination of the basic friction angle of rock surfaces by tilt tests[J]. Rock Mechanics and Rock Engineering, 2018, 51(4): 989−1004.

[53] ULUSAY R, KARAKUL H. Assessment of basic friction angles of various rock types from Turkey under dry, wet and submerged conditions and some considerations on tilt testing[J]. Bulletin of Engineering Geology and the Environment, 2016, 75(4): 1683−1699.

[54] ZHONG Z, YONG R, TANG H M, et al. Experimental studies on the interaction mechanism of landslide stabilizing piles and sandwich-type bedrock[J]. Landslides, 2021, 18(4): 1369−1386.